ADVANCED MATERIALS
www.advmat.de

Interstitial Oxygen Acts as Electronic Buffer Stabilizing High-Entropy Alloys for Trifunctional Electrocatalysis

Xiaoxiao Zou, Xinyu Zhao, Bohuai Pang, Hang Ma, Kun Zeng, Songsong Zhi, and Hong Guo**

Understanding the effect of elements' oxygen affinity is essential for comprehending high-entropy alloys' (HEAs) complete properties. However, the origin of HEAs' oxygen-containing structure and stability remains poorly understood, primarily due to their diverse components, hindering synthesis and analysis. Herein, the O-doping HEAs (HEA-O) have demonstrated outstanding performance and stability in electrolyzed water and Zinc–air batteries which can be reassembled after being stable for more than 1600 h when the zinc consumption is over. The experiment and DFT simulation demonstrate that Cr with strong oxygen affinity can introduce more oxygen into the system of HEAs. Consequently, interstitial oxygens act as electronic buffers making the binding energy of other metal elements move to a higher level. Additionally, O-doping lowers the d-band center promoting electrochemical activity and increasing vacancy formation energies of metal active sites leading to super stability. The study provides significant insights into the design and comprehension of interstitial oxygen-doped HEAs.

1. Introduction

High-entropy alloys (HEAs) showing strong benefits in electrocatalysis are candidates for industrial applications with high activity and enhanced durability due to their significant virtues.[1–5] Most recently, interstitial O-doping penetrating the lattice gap improved the tensile strength and plasticity of HEAs significantly, providing a fresh understanding of interstitial oxygen reinforcement.[6] The interstitial oxygen does not occupy the lattice sites, resulting in the original structure of HEAs, which maintains its excellent characteristics. Additionally, understanding the role of interstitial oxygen doping is essential for comprehending HEAs' complete properties.[7,8] However, it is difficult to pay attention to interstitial oxygen doping because of the complex composition and synthesis of HEAs, especially the effect of strong oxygen-affinity elements on interstitial oxygen doping in HEAs is less reported.

The reasons for interstitial oxygen incorporation being inevitable yet often overlooked are as follows: First, common methods used to mitigate ineffective oxidation are through ultrahigh vacuum or protective gas atmosphere due to oxygen being omnipresent, but perfection rarely attainable. Second, oxygen has small atomic radii that easily infiltrate the lattice in interstitial doping, resulting in an interstitial solid solution and not easily detected. Third, clean materials are prone to oxygen functional group adsorption on the surface upon exposure to air, leading to oxygen error in instrument analysis.[6,9–11] Consequently, most work has focused on the change in active sites brought about by HEAs' element type shifts and superior performance by its high-entropy effects, especially in the field of electrocatalysis,[12,13] with minimal attention paid to the presence of oxygen in the HEAs system.

Herein, we ingeniously integrate a unique self-supporting trifunctional catalytic electrode with Cr, Mn, Fe, Ni, and Pt HEAs nanoparticles (HEA-O) as **Scheme 1**. The Cr with strong oxygen-affinity makes more oxygen atoms acting as electronic buffers in HEAs resulting in the binding energy of each element moving higher than MnFeNiPt. Furthermore, X-ray absorption fine structure (XAFS) characterization and density functional theories (DFT) simulation findings demonstrate Cr's superior ability to bond and engage oxygen, making it an ideal candidate for stable O-doped HEAs. Electrons of the HEA-O metal atoms are redistributed due to varying degrees of migration to the O atom and providing vacant orbitals. Therefore, the inclusion of O-doping contributes to lowering the d-band center and promoting electrochemical activity. In addition, O-doping increased vacancy formation energies of metal active sites for HEA-O, which has the

X. Zou, X. Zhao, B. Pang, K. Zeng, H. Guo
School of Materials and Energy
International Joint Research Center for Advanced Energy Materials of Yunnan Province
Yunnan University
Kunming 650091, P. R. China
E-mail: guohong@ynu.edu.cn
H. Ma
R & D Center
Yunnan Yuntianhua Co., Ltd
Kunming 650228, P. R. China
S. Zhi
School of Environment
Henan Normal University
Key Laboratory of Yellow River and Huai River Water Environment and Pollution Control
Ministry of Education
Xinxiang, Henan 453007, P. R. China
E-mail: 1903183057@stu.htu.edu.cn

The ORCID identification number(s) for the author(s) of this article can be found under https://doi.org/10.1002/adma.202412954

DOI: 10.1002/adma.202412954

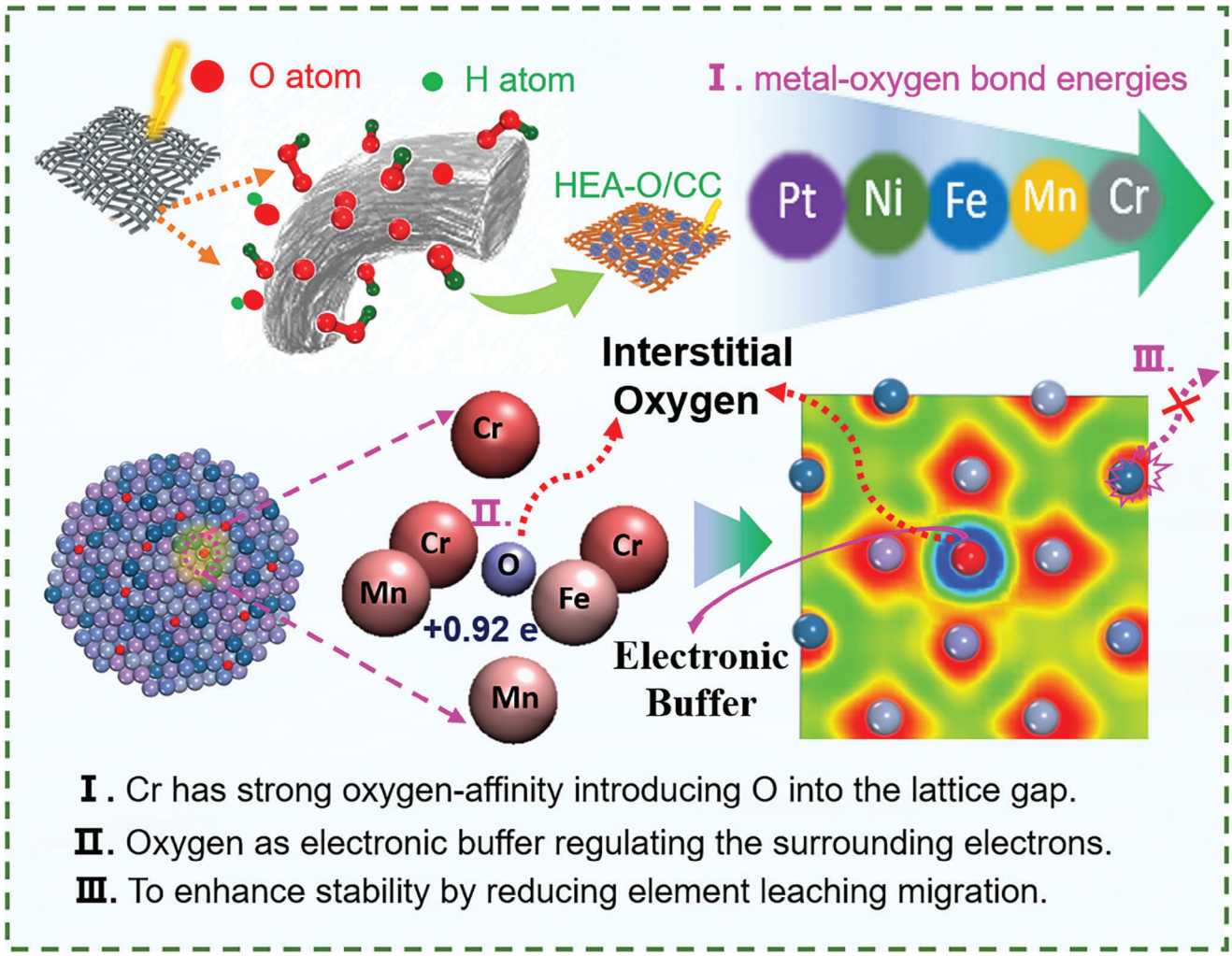

Scheme 1. Schematic illustration of the synthesis process and mechanism of HEA-O.

potential to enhance stability by reducing element leaching migration. Finally, all of these make HEA-O have excellent properties and enhanced stability of oxygen evolution (OER), hydrogen evolution (HER), and oxygen reduction (ORR) reactions under alkaline conditions, which has demonstrated outstanding performance and stability in electrolyzed water and Zinc–air batteries (ZABs). Thus, the results of the work prove that the introduction of pro-oxy elements into HEAs resulted in interstitial O-doping. As O atoms possess strong electronegativity, their introduction can act as an electronic buffer, enabling the redistribution of charges in the HEAs system, reinforcing bonding between adjacent elements, and realizing interstitial solid solution strengthening. The study provides significant insights into the design and comprehension of interstitial oxygen-doped HEAs.

2. Results and Discussion

As shown in Scheme 1, the carbon cloth (CC) was pretreated by the joule heating to surface enrichment with oxygen-bearing functional groups elevating salt dispersion, and then the joule-treated CC(JCC) was immersed in various chloride solutions, after drying, the JCC was subjected to joule heat treatment under protective gas, a self-supporting electrode loaded with HEA-O on CC was obtained. Figure S1 (Supporting Information) comparison of scanning electron microscope (SEM) of different magnification and contact angle measurements of CC under different treatment conditions shows that the CC pretreated by the Joule method has stronger hydrophilicity than the CC pretreated by strong acid.[14] Figure S2a (Supporting Information) shows the four-probe resistance test of CC under different treatment conditions. It can be seen that the CC pretreated by strong acid and joule method has no direct effect on the electrical conductivity of CC, but still maintains good electrical conductivity. The $I_{D(defect)}/I_{G(graphite)}$ value of the Raman in Figure S2b (Supporting Information) also shows that the JCC has more defects than the strong acid-treated CC, demonstrating that the joule heating method is faster and safer than the strong acid pretreatment.

Figure 1a is a spherical aberration-corrected transmission electron microscopy(AC-TEM) image and corresponding geometric phase analysis (GPA) of HEA-O particles, which shows both shear strain and axial strain (compression strain or tensile strain) occur in HEA-O.[15,16] Figure 1b of energy dispersive

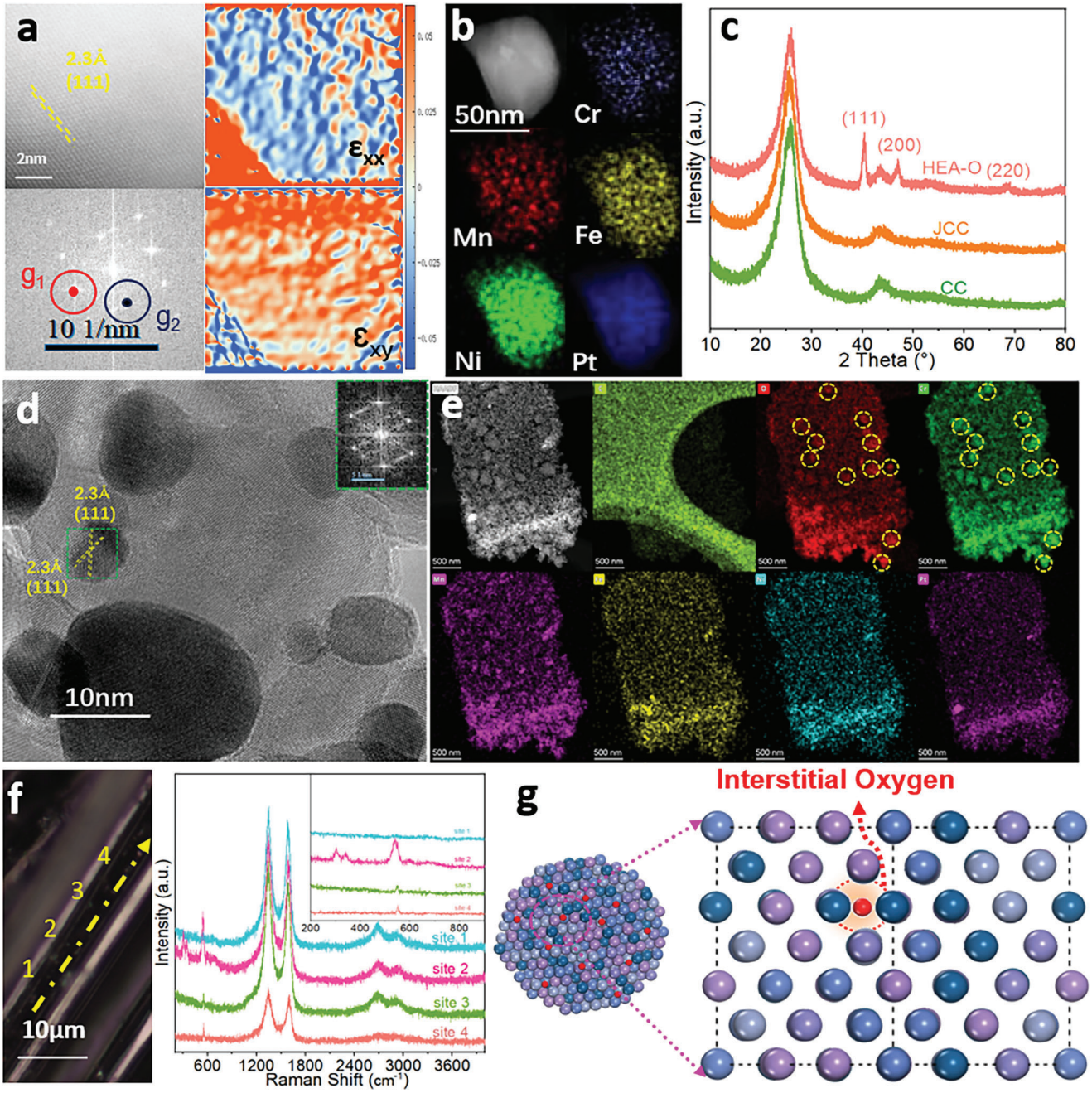

Figure 1. a) AC-STEM image of HEA-O and corresponding GPA images, and b) EDS maps of Cr, Mn, Fe, Ni, and Pt, c) XRD of CC, JCC, and HEA-O, d) HRTEM images (insert FFT patterns of the relevant parts), and e) EDS mapping of C, O, Cr, Mn, Fe, Ni, and Pt, f) the image of HEA-O under a Raman microscope (the right diagram shows the Raman spectra of the points labeled 1–4 and g) Diagram of the model structure for HEA-O.

spectroscopy (EDS) shows that the HEA-O nanoparticles are evenly formed by Cr, Mn, Fe, Ni, and Pt. Figure 1c shows the X-ray diffraction (XRD) of CC, JCC, and HEA-O. It can be seen that the HEA-O has an obvious Face Center Cubic (FCC) structure peak and is a single-phase solid solution. Figure 1d shows a higher magnification transmission electron microscope (TEM) image of HEA-O, inset with a Fast Fourier transform (FFT) dot image of the corresponding portion, and the lattice spacing (0.23 nm) is the same as Figure 1a. These results are consistent with the XRD results indicating the HEAs structure of HEA-O.[17] Figure 1e is the dark-field EDS of the various elements in a large range, showing that the HEA-O has very little carbon and that the other elements are evenly distributed. In addition, O, and Cr elements have a strong association. Figure 1f the image of HEA-O under a Raman microscope shows a relatively compact reflective surface, the inset shows the Raman spectra of the points labeled 1–4, indicating the presence of a small number of oxygen-containing bonds in HEA-O,[18] which also corresponds to the EDS of O

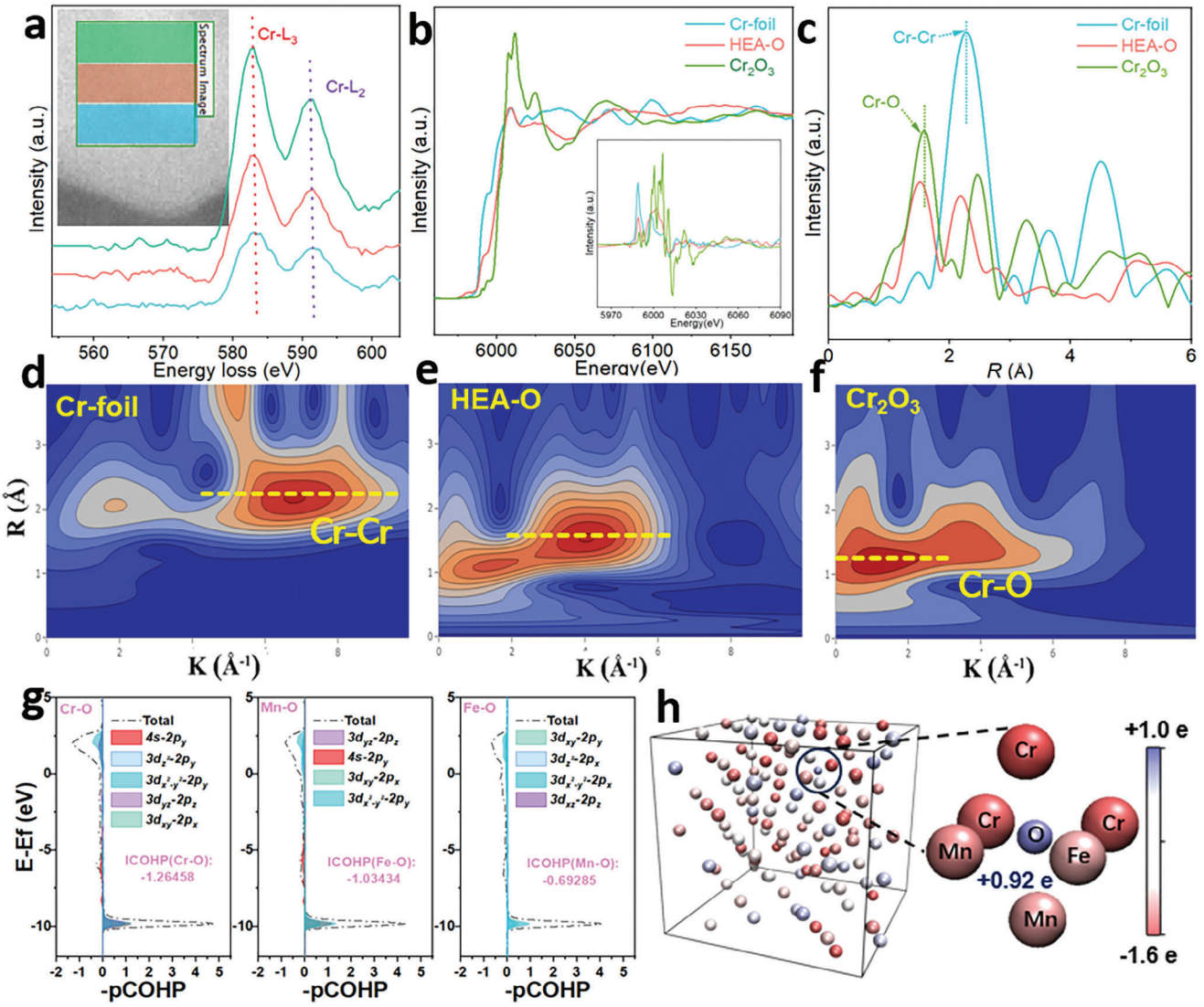

Figure 2. a) EELS spectrum for Cr and b) XAS spectra and corresponding derivative curves for Cr K-edge, c) FT-EXAFS spectra d–f) wavelet transform of Cr-foil, HEA-O, and Cr_2O_3. g)COHP analysis for Cr-O, Mn-O, and Fe—O of the HEA-O Molde h) The bulk structure of HEA-O is colored by atom charge (negative charge is colored in blue and positive charge is colored in red).

species. It is inferred that the introduction of Cr causes O to enter into the lattice gap of HEAs. Therefore, 100 random theoretical structures of HEA were generated and the most thermodynamically stable model was selected for doping with O atom as the structure of HEA-O to DFT simulation. (Figure 1g; Figures S12 and S13, Supporting Information).

To gain a better understanding of the changes in the local electronic structure and coordination environment of Cr atoms in highly heterogeneous elements in HEAs, electron energy loss spectroscopy (EELS) and synchrotron radiation XAFS of HEA-O were measured.[19] As can be seen from the EELS spectra (**Figure 2a**) of different parts of HEA-O particles, the peaks of Cr L_3 and Cr L_2 move toward the high-energy direction closer to the particle edge, indicating the appearance of more external oxidation states. Figure 2b shows the fine XAS of Cr-foil, HEA-O, and Cr_2O_3, it can be seen that Cr in HEA-O has a different absorption spectrum from that of Cr-foil and Cr_2O_3, but has a strong similarity to Cr-foil.[20] Figure 2c shows the contrast R-space information and map of wavelet transform based on Morlet wavelet signal (Figure 2d–f) is extended obtained by Fourier transform X-ray absorption fine structure (FT-EXAFS), indicating the presence of both Cr—Cr and Cr—O bonds.[21] From the above results of EELS and XAS, it can be concluded that Cr with strong oxygen affinity will bring O atoms into the HEAs system. Furthermore, we employed crystal orbital Hamiltonian populations (COHP) to investigate the interaction of metal-O (M—O) bonds in HEA-O by DFT simulation in Figure 2g. The result revealed that hybridized electrons occupy predominantly bonding orbitals, indicating the formation of stable interstitial HEAs. Additionally, negative integrated COHP (ICOHP) values signify a stronger Cr—O (−1.26458) bond than Mn—O (−1.03434) or Fe—O (−0.69285).[22,23] The diagram in Figure 2h exemplifies O's potent

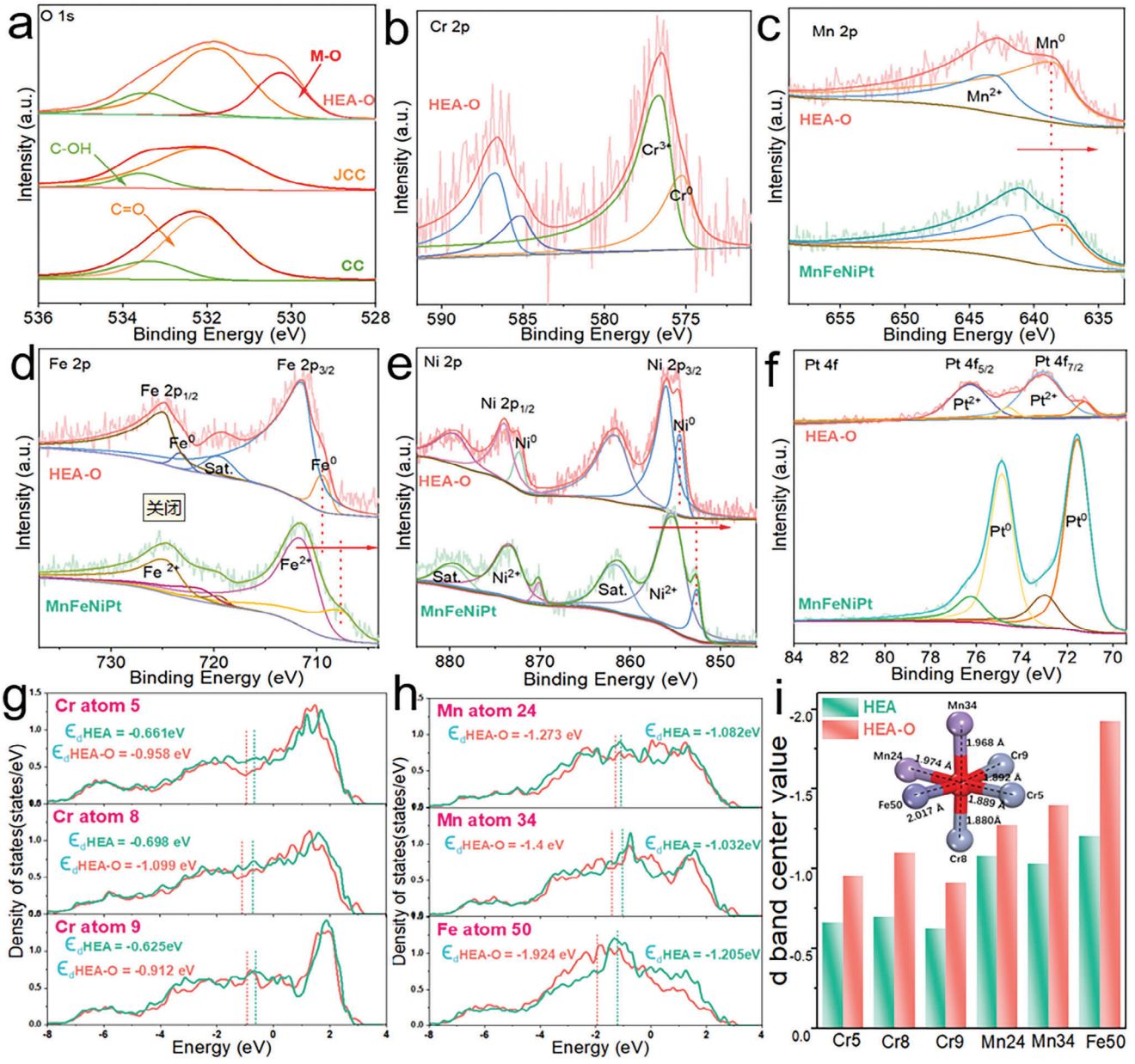

Figure 3. XPS analysis a) O1s spectrum of CC, JCC, and HEA-O, b) Cr 2p spectrum of HEA-O. c)Mn 2p spectrum, d)Fe 2p spectrum, e)Ni 2p spectrum, and f) Pt 4f spectrum of HEA-O and MnFeNiPt. g,h) LDOS for O atoms near differing site elements in the model of HEA and HEA-O. i) the d-band center of HEA and HEA-O, and inset featuring a model diagram with the value of bond length.

electron donor capacity. As we can see, the electron migration from the six first shell metal atoms induce charge redistribution and creates vacant orbitals at metallic sites for additional electrons within the octahedron. This change in the electronic state suggested that the introduction of Cr has led to electronically strong interactions with electron transfer between O and first-shell metal.

Figure 3a shows the X-ray photoelectron spectroscopy (XPS) fine spectra of O1s in CC, JCC, and HEA-O, respectively. The results demonstrate a significantly enhanced M—O bond energy in HEA-O compared to CC and JCC.[24] From the peak-splitting results in Figure 3b–f, it can be shown that each element will have the corresponding oxidation valence state because XPS is a surface test, this phenomenon is quite common corresponding to the previous results.[25,26] In addition, we compared the peak position shift of the samples without adding Cr. We can see that the metal valence states of Mn, Fe, and Ni in HEA-O move toward high binding energy after adding Cr, which means the loss of electrons.[27] For Pt, the peak strength of the directly oxidized state is higher than the peak strength of the metallic state, further indicating that the binding energy moves toward the higher binding energy. This indicated that Cr can bring Oxygen to the HEAs and affect the electronic structure of the nanoparticles. Because the intrinsic activity of the catalyst is related to the change of the

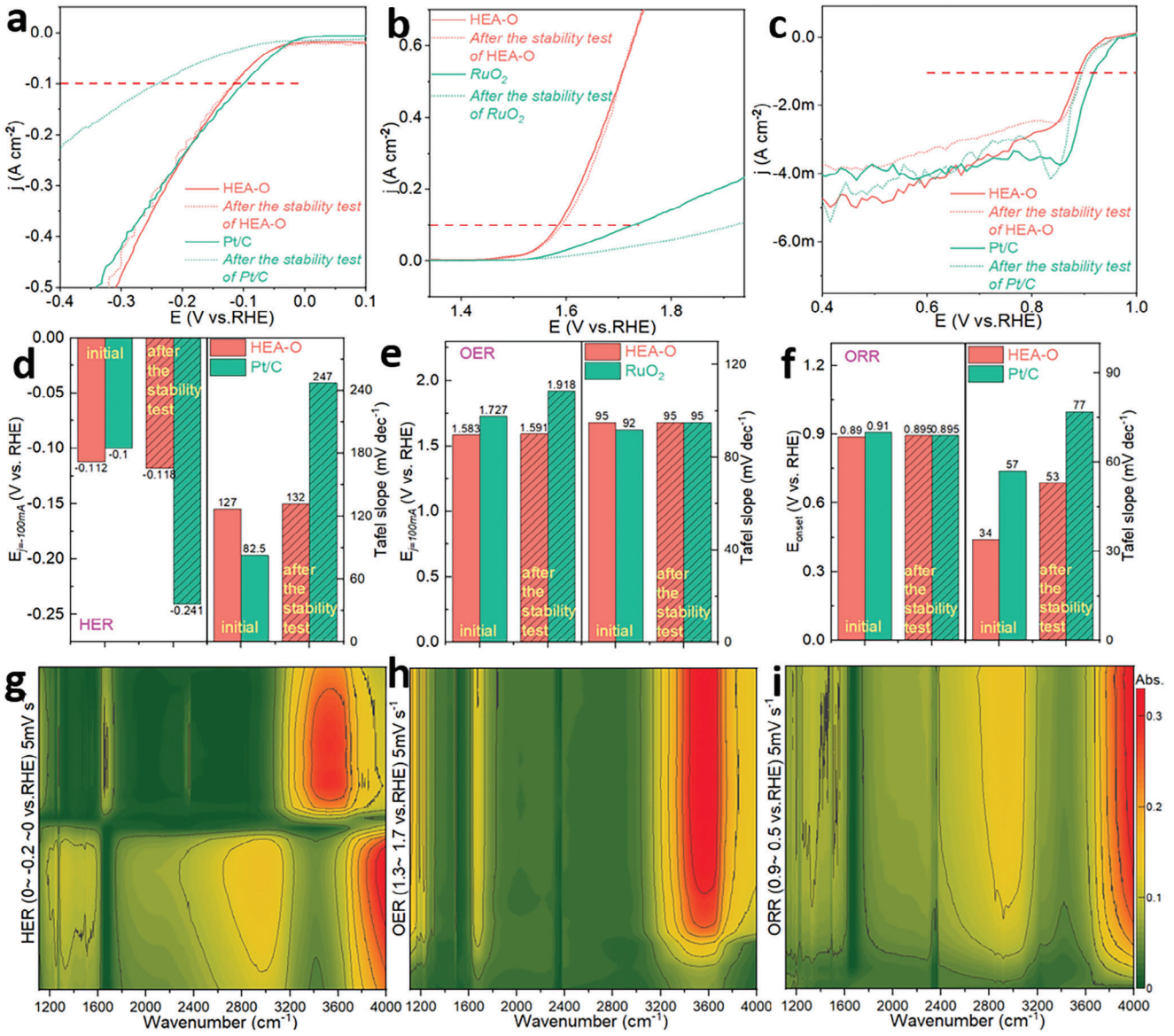

Figure 4. a–c) HER, OER and ORR polarization LSV curves, d) Tafel plots and $E_{j=100}$ in HER, e) Tafel plots and $E_{j=100}$ in OER, and f) Tafel plots and onset potential for HEA-O and commercial catalyst, g– i) in situ infrared 2D contour image for the HER, OER and ORR.

d-band center caused by the change of its electronic structure to a great extent. Subsequently, the local density of state (LDOS) changes before and after doping O was calculated. Obvious from Figure 3g,h, HEA-O's d-band center significantly drops, signifying weak bonding with the reaction intermediate, facilitating the desorption and mass transfer of these intermediates for boosted catalytic activity.[28] Figure 3i illustrations depict the Cr—O (1.887 Å) bond possessing the shortest length, lower than Mn—O (1.971 Å) and Fe—O (1.974 Å) average bond lengths. The experimental characterization and theoretical evidence reiterate Cr's superior affinity for oxygen and its bonding potential. Consequently, the incorporation of Cr positively influences O-doped interstitial stability within HEAs systems.

To gain a better understanding of the performance of the different element combinations of the self-supporting electrode prepared by this method. As shown in **Figure** 4a–c are the polarization curves by linear scanning voltammetry (LSV) of HEA-O self-supporting electrode and commercial catalyst in 1 M KOH in HER, OER, and ORR, respectively.[29] It can be seen that the HEA-O self-supporting electrode has good performance and strong cyclic stability. Figure 4d shows a potential value of 100 mA cm^{-2} and a Tafel slope value for the pre-and post-cyclic current density of HEA-O and commercial Pt/C during HER, further demonstrating the good cyclic stability of HEA-O. Figure 4e shows a potential value and a Tafel slope value of 100 mA cm^{-2} for both HEA-O and commercial RuO_2 before and after cycling in the OER potential, again illustrating the superior OER performance of HEA-O over commercial RuO_2. Figure 4f shows the pre-and post-cyclic onset potential and Tafel slope values of HEA-O and commercial Pt/C during ORR, illustrating the good

cyclic stability of HEA-O in ORR. At the same time, the performance of HER, OER, and ORR of self-supporting electrodes of four metals and three metal combinations is compared in Figure S8a–f (Supporting Information), it is further proved that the high-entropy combination of HEA-O can bring the best trifunctional performance. Mass transfer is an important factor that should be considered when designing electrocatalysts. Figure S8g (Supporting Information) shows the electrochemical impedance spectroscopy (EIS) measurements of the different electrodes showing that the prepared HEA-O electrode has a minimum charge transfer resistance, speeding up the slow chemical kinetics step, the important role of self-supporting in the catalytic process is further explained. Figures S9a–c (Supporting Information) are the CV curves tested for the non-faraday region of the different electrodes, and Figure S9d (Supporting Information) is the contrast value of the ECSA calculated from the above double-layer capacitance (C_{dl}, C_{dl} was the slope to reveal ECSA) from the calculated values in the figures, it can be seen that commercial Pt/C has the largest ECSA and RuO_2 has the smallest ECSA. From this result, it can be compared that HEA-O has higher catalytic activity although ECSA is smaller than Pt/C, which shows that the catalytic activity of HEA-O is higher per unit area.

To monitor the generation of intermediates in different reaction processes under primary reaction conditions and to further understand the catalytic process mechanism of the high-entropy self-supporting electrode, Figure 4g–i are counter graphs of in situ infrared signals of HEA-O self-supporting in HER, OER, and ORR reaction regions.[30] Figure 4g, for the HER, the H_2O peaks at 3000–4000$^-$ and 1600–1800 cm^{-1} became weaker when the potential decreased, and stronger when the potential increased, the results show that the water consumption process in alkaline.[31] At 1290 cm^{-1}, the strong peaks were also captured, which further indicated that the HER process in an alkaline environment was a weak bonding peak of dissociation and collision with water.[32] The complementary changes of ORR and OER can be seen in Figures 4h,i, which confirm the reverse process of the two reactions. The H_2O peaks at 3000–4000$^-$ and 1600–1800 cm^{-1} in the ORR reaction range were the weakening mode, which indicated that the alkaline ORR was a process of water consumption. With the oxygen reduction process, a small peak appeared at 1280 cm^{-1}, which was classified as *OOH.[33] For the OER reaction range, the peak height of H_2O at 3000-4000$^-$ and 1600–1800 cm^{-1} increased significantly, which indicated the formation of surface water in the alkaline OER process, the enhancement of *OOH peak was also observed at 1111–1250 cm^{-1}. The different peak positions of *OOH in the two reaction processes also indicated the opposite process of ORR and OER, the bond length becomes shorter to generate O_2, while the OER peak moves to a lower wavenumber, and the bond length becomes longer, causing O_2 bonds to open and consume O_2. The above changes were observed by the in situ infrared experiment under the condition of simulating the in situ conditions, which reflected the formation and consumption of substances in the three reactions more truly.

To investigate the origin of HEA-O's stability, we initially analyzed its electronic structure's impact on stability.[34] As shown in **Figure** 5a, the electronic localization function (ELF) before and after O-doping was compared to assess the effect of this doping on HEAs systems. This analysis revealed enhanced electron localization around the O dopant, inducing varying degrees of electron density alterations in adjacent elements. According to the calculated results, the charge density tends to accumulate around the O-doping sites in HEA-O. Furthermore, vacancy formation energy ($E_{vacancy}$) emerges as a powerful indicator of system stability due to element dissolution capacity being a determinant of material stability. The $E_{vacancy}$ for various sites before and after O-doping – clearly shows that HEA-O boasts higher $E_{vacancy}$ than HEA does, reinforcing the structural robustness of HEA-O (Figure 5b).

We finally verified the stability of HEA-O on a device through experimentation. As shown in Figure 5c by comparing the LSV of the assembled water electrolysis device, it can be seen that HEA-O is superior to the commercial catalyst and maintains good stability. Figure 5d shows the performance of HEA-O during the long cycle of electrolyzing water. It can be seen that HEA-O performs better when the cathode and anode are exchanged and remain stable after a while, stable electrolytic potential was maintained over 20 days. Figure 5e shows that the assembled liquid ZABs show that HEA-O can maintain good charge–discharge performance after cycling for 1600 h, and ΔE is almost always maintained at 0.72 V, Figure S10b (Supporting Information) is a cyclic test of HEA-O assembled liquid ZAB at 10 mA cm^{-2}, showing that its ΔE is maintained at ≈0.86 V and is stable. At the end of the cycle, replace the zinc with a new one, as shown in Figure S10c (Supporting Information), the ZABs of the secondary cycle can still maintain a certain degree of cycling stability. The solid-state ZABs were then assembled, as shown in Figure 5f, also showing that HEA-O has good cyclic stability after 33 h of solid electrolyte breakdown, the cathode electrode can be reassembled into a solid-state ZABs as shown in Figure S10d (Supporting Information), and the cycle performance can still be maintained. From the above cycle test results, it can be seen that the HEA-O self-supporting electrode has excellent cycle stability, which is due to the strong stability of high-entropy and the characteristics of a self-supporting process.

To further understand the source of the stability of HEA-O, XRD tests were carried out on the electrodes after different catalysts as shown in Figure S11a (Supporting Information), after each catalytic reaction, the FCC peak of HEA-O became narrower, which indicated that the particle size of HEA-O became larger after recycling.[35] The electrode was then sonicated and the material was tested by TEM, as shown in Figure S11b (Supporting Information). The high-entropy particles were tightly coated with carbon, and some of the particles became larger, this corresponds to the XRD results after cycling. Figure S11c (Supporting Information) is an EDS test of the post-cycling sample, which further reveals the carbon layer signal, indicating that the carbon is tightly packed with HEAs after the catalytic cycling and that the various elements in the particles are remarkably evenly distributed, you can see that the particles are getting larger. From the test results of the above cycles, it can be concluded that the self-supporting high-entropy electrode made by this method can bond more firmly with the carbon carrier after a long cycle, the method makes the active material not easy to fall off.

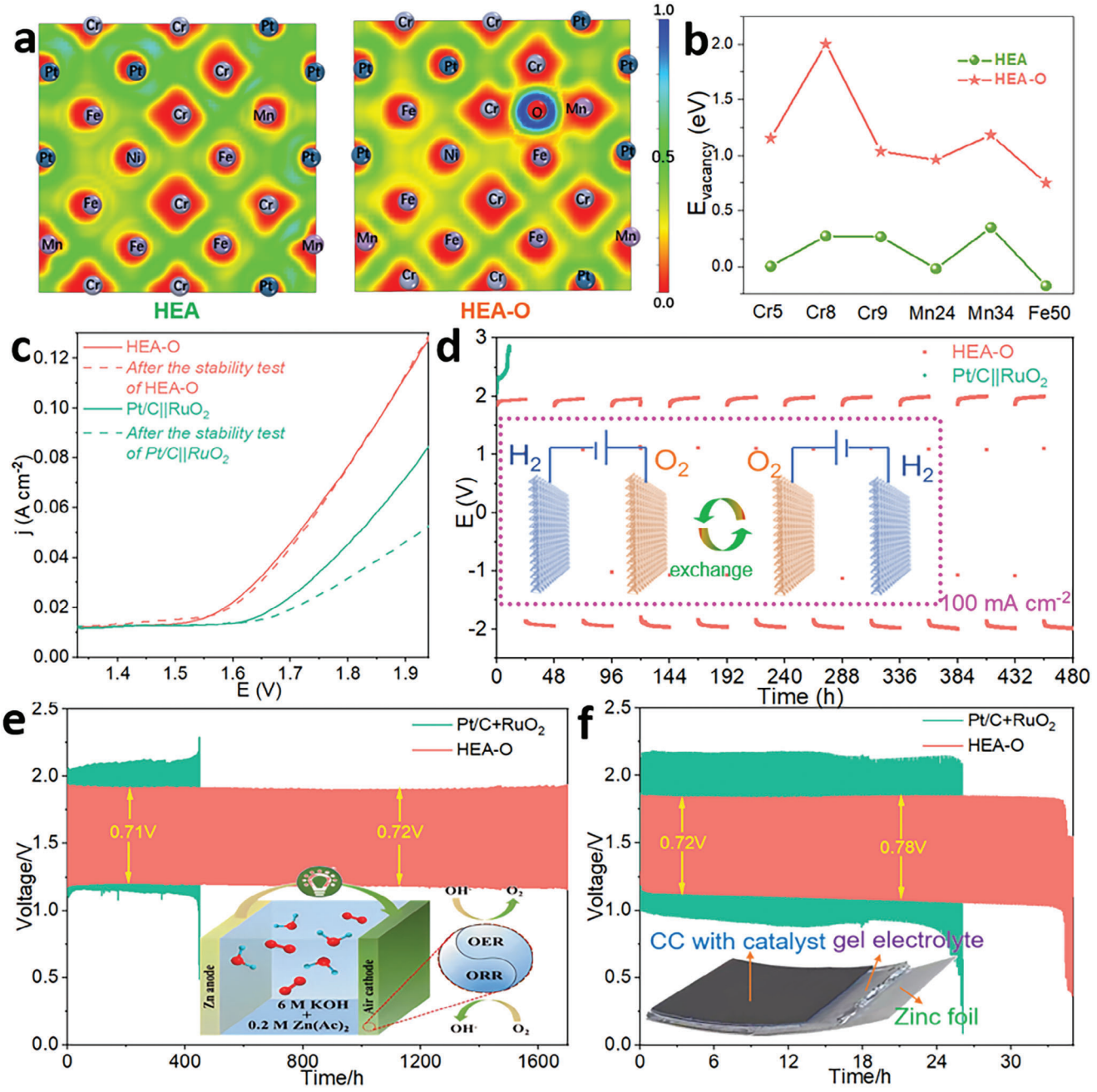

Figure 5. a) ELF for HEA and HEA-O, b) Vacancy formation energy ($E_{vacancy}$) for different sites of HEA and HEA-O c)Polarization curves for water splitting, and (d)water splitting stability test of HEA-O and (-) Pt/C||RuO_2(+). Discharge–charge cycling curves of the e) liquid ZAB and f) solid ZAB for HEA-O and Pt/C+ RuO_2.

3. Conclusion

In this thesis, the self-supporting HEA-O synthesized by the rapid joule heating method has good versatility and can be repeatedly and stably utilized in water electrolysis and ZABs devices. From the experimental and theoretical calculations results, it can be seen that the Cr element with strong oxygen affinity can introduce oxygen atoms into the HEAs system. Interstitial oxygen acts as an electronic buffer making the binding energy of other metal elements move to a higher level and lower the d-band center position. Therefore, the electronic structure of each element is changed comprehensively, and the stability of the system is enhanced. This study exhibits that new insight into the elements with strong oxygen-affinity for O-doping in the HEAs system have vital effects, and introduce practical ideas for HEAs' application in electrocatalysis.

4. Experimental Section

The Preparation of HEA-O and Other Samples: CC was ultrasonic washed with deionized water before use and then ultrasonic washed in ethanol. After drying, CC was cut to a size of 2×3 cm^{-1}, CC is electrified in a fast mode, and the surface of the electrified CC becomes hydrophilic. The model of Joule heating equipment was CIS-JH3.3-P (In situ High-tech). The Joule heat-treated CC (JCC) in the air was cut to a size of 1×3 cm^{-1}, the JCC was then placed in an ethanol solution of 0.1 M of $CrCl_2{\cdot}6H_2O$, $MnCl_2{\cdot}4H_2O$, $FeCl_3$, and $NiCl_2$, and 0.05 M $PtCl_2$ (Since Pt has a much lower vapor pressure compared to others and JCC having a small specific surface area and reacting on the surface), soaked for 1 min to remove and dry. The Joule heat-treated CC was cut to a size of 1×1.5 cm^{-1} (the mass had been weighed) and then placed between folded carbon paper, which was sandwiched on either side of the graphite electrode, then, using a pulse mode (One 40V 400A and 4 ms pulse), in a protected atmosphere, a pulse was generated to obtain a high-entropy nanoparticle-loaded CC. After washing and drying, the weight minus the mass of the treated CC was the mass of the nanoparticles loaded on it (≈1 mg).

Strong Acid Pretreated CC: 2 g CC was added to the mixed solution of 10 mL concentrated nitric acid and 30 mL concentrated sulfuric acid, stirred at room temperature for 2 h, then slowly added deionized water to the total volume of 120 mL while stirring, the CC was soaked and washed with 5% hydrochloric acid. Then CC was soaked and washed with deionized water, and finally soaked and washed with ethanol dried for use.

Theoretical Simulations: The DFT was carried out by using the Vienna Ab initio Simulation Package.[36] To identify a reasonable geometry, a set of 100 random geometries was scanned in terms of total energy. After this screening, the bulk structure with the highest stability was selected for further optimization. The Perdew–Burke–Ernzerh of generalized-gradient approximation functional was used to describe the interaction between electrons.[37] The energy cutoff was set to 500 eV. The Gamma-centered k-points grid was set to be $3 \times 3 \times 3$ for all the calculations. The convergence threshold for energy and force was set to be less than 10^{-5} eV and 0.02 eV $Å^{-1}$. The DFT-D3 method was adopted to evaluate the van der Waals interaction.[38] Spin polarization was considered in all calculations. The bonding/antibonding population between the metal and O-doping in bulk structure was analyzed using the COHP.[39] The atomic structures were visualized by the VESTA· program.[40] The charge density difference, LDOS, and *d*-band center were calculated using the VASPKIT toolkit.[41]

The other experimental sections for characterization, in situ characterization, and electrochemical tests are shown in Supporting Information.

Supporting Information

Supporting Information is available from the Wiley Online Library or from the author.

Acknowledgements

The authors would like to acknowledge the financial support provided by the Major Science and Technology Projects of Yunnan Province (202302AB080019-3), National Natural Science Foundation of Yunnan Province (202301AS070040), the Yunnan University's Research Innovation Fund for Graduate Students (KC-23233757), Laboratory of Solid-State Ions for Green Energy of Yunnan University, the Analysis and Measurements Center of Yunnan University for the sample testing service, the Electron Microscope Center of Yunnan University for the support of this work. The authors would like to thank the Anhui Absorption Spectroscopy Analysis Instrument Co, Ltd. for XAFS measurements, and Shiyanjia Lab (www.shiyanjia.com) for the XPS test.

Conflict of Interest

The authors declare no conflict of interest.

Data Availability Statement

Research data are not shared.

Keywords

electronic buffer, high-entropy alloys, interstitial oxygen, trifunctional electrocatalysis

Received: August 30, 2024
Revised: October 14, 2024
Published online:

[1] Y. Sun, W. Zhang, Q. Zhang, Y. Li, L. Gu, S. Guo, *Matter* **2023**, *6*, 193.
[2] Y. Yao, Z. Huang, P. Xie, S. D. Lacey, R. J. Jacob, H. Xie, F. Chen, A. Nie, T. Pu, M. Rehwoldt, D. Yu, M. R. Zachariah, C. Wang, R. Shahbazian-Yassar, J. Li, L. Hu, *Science* **2018**, *359*, 1489.
[3] S. Schweidler, M. Botros, F. Strauss, Q. Wang, Y. Ma, L. Velasco, G. Cadilha Marques, A. Sarkar, C. Kübel, H. Hahn, J. Aghassi-Hagmann, T. Brezesinski, B. Breitung, *Nat. Rev. Mater.* **2024**, *9*, 266.
[4] J. T. Ren, L. Chen, H. Y. Wang, Z. Y. Yuan, *Chem. Soc. Rev.* **2023**, *52*, 8319.
[5] Y. Yao, Q. Dong, A. Brozena, J. Luo, J. Miao, M. Chi, C. Wang, I. G. Kevrekidis, Z. J. Ren, J. Greeley, G. Wang, A. Anapolsky, L. Hu, *Science* **2022**, *376*, eabn3103.
[6] Z. Lei, X. Liu, Y. Wu, H. Wang, S. Jiang, S. Wang, X. Hui, Y. Wu, B. Gault, P. Kontis, D. Raabe, L. Gu, Q. Zhang, H. Chen, H. Wang, J. Liu, K. An, Q. Zeng, T. G. Nieh, Z. Lu, *Nature* **2018**, *563*, 546.
[7] B. Gwalani, A. Martin, E. Kautz, B. Guo, S. V. Lambeets, M. Olszta, A. K. Battu, A. Malakar, F. Yang, J. Guo, S. Thevuthasan, R. Li, A. Amassian, M. Thuo, A. Devaraj, *Nat. Commun.* **2024**, *15*, 5026.
[8] X. L. Z. H. U. Chenhui, L. I. U. Meijun, G. U. O. Mingyi, *Chin. J. Eng.* **2023**, *45*, 1459.
[9] D. Cui, Y. Zhang, L. Liu, Y. Li, L. Wang, Z. Wang, J. Li, J. Wang, F. He, *J. Mater. Sci. Technol.* **2023**, *157*, 11.
[10] S. Jiang, H. Wang, Y. Wu, X. Liu, H. Chen, M. Yao, B. Gault, D. Ponge, D. Raabe, A. Hirata, M. Chen, Y. Wang, Z. Lu, *Nature* **2017**, *544*, 460.
[11] L. K. Iroc, O. U. Tukac, B. B. Tanrisevdi, O. El-Atwani, M. A. Tunes, Y. E. Kalay, E. Aydogan, *Mater. Des.* **2022**, *223*, 111239.
[12] Y. Li, Y. Liao, J. Zhang, E. Huang, L. Ji, Z. Zhang, R. Zhao, Z. Zhang, B. Yang, Y. Zhang, B. Xu, G. Qin, X. Zhang, *Angew. Chem., Int. Ed.* **2021**, *60*, 27113.
[13] H. Li, Y. Han, H. Zhao, W. Qi, D. Zhang, Y. Yu, W. Cai, S. Li, J. Lai, B. Huang, L. Wang, *Nat. Commun.* **2020**, *11*, 5473.
[14] X. Li, F. Chen, B. Zhao, S. Zhang, X. Zheng, Y. Wang, X. Jin, C. Dai, J. Wang, J. Xie, Z. Zhang, Y. Zhao, *Nanomicro Lett* **2023**, *15*, 32.
[15] S. Feng, Z. Xu, *Materials* **2021**, *14*, 4460.
[16] S. Hao, H. Sheng, M. Liu, J. Huang, G. Zheng, F. Zhang, X. Liu, Z. Su, J. Hu, Y. Qian, L. Zhou, Y. He, B. Song, L. Lei, X. Zhang, S. Jin, *Nat. Nanotechnol.* **2021**, *16*, 1371.
[17] L. Tao, M. Sun, Y. Zhou, M. Luo, F. Lv, M. Li, Q. Zhang, L. Gu, B. Huang, S. Guo, *J. Am. Chem. Soc.* **2022**, *144*, 10582.
[18] J. Hu, T. Q. Guo, X. Y. Zhong, J. Li, Y. J. Mei, C. X. Zhang, Y. B. Feng, M. Z. Sun, L. J. Meng, Z. Y. Wang, B. L. Huang, L. B. Zhang, Z. C. Wang, *Adv. Mater.* **2024**, *36*, 2310918.
[19] J. Zhao, Z. Wang, X. Fang, L. Yang, C. Wu, W. Gan, Y. Zhou, L. Shan, Y. Lin, *J. Alloys Compd.* **2023**, *966*, 171535.
[20] S. Xu, D. Jiao, X. Ruan, Z. Jin, Y. Qiu, Z. Feng, L. Zheng, J. Fan, W. Zheng, X. Cui, *Adv. Funct. Mater.* **2024**, *34*, 2401265.
[21] K. A. Moltved, K. P. Kepp, *J. Phys. Chem. C* **2019**, *123*, 18432.
[22] J. Schumann, M. Stamatakis, A. Michaelides, R. Réocreux, *Nat. Chem.* **2024**, *16*, 749.

[23] J. Zhu, M. Xiao, D. Ren, R. Gao, X. Liu, Z. Zhang, D. Luo, W. Xing, D. Su, A. Yu, Z. Chen, *J. Am. Chem. Soc.* **2022**, *144*, 9661.
[24] P. Yang, Y. Shi, T. Xia, Z. Jiang, X. Ren, L. Liang, Q. Shao, K. Zhu, *J. Alloys Compd.* **2023**, *938*, 168582.
[25] Z. y. Mei, G. Zhao, C. Xia, S. Cai, Q. Jing, X. Sheng, H. Wang, X. Zou, L. Wang, H. Guo, B. Y. Xia, *Angew. Chem., Int. Ed.* **2023**, *62*, 202303871.
[26] X. X. Zou, J. Y. Xie, Z. Y. Mei, Q. Jing, X. L. Sheng, C. H. Zhang, Y. X. Yang, M. J. Sun, F. T. Ren, L. L. Wang, T. W. He, Y. C. Kong, H. Guo, *Proc. Natl. Acad. Sci. U.S.A.* **2024**, *121*, 2313239121.
[27] H. Li, H. Huang, Y. Chen, F. Lai, H. Fu, L. Zhang, N. Zhang, S. Bai, T. Liu, *Adv. Mater.* **2022**, *35*, 2209242.
[28] H. Huang, C. Chen, C. C. Chang, F. Lai, S. Liu, H. Fu, Y. Chen, H. Li, W. H. Huang, N. Zhang, T. Liu, *Adv. Mater.* **2024**, *36*, 2314142.
[29] J. Hu, Y. Qin, H. Sun, Y. Ma, L. Lin, Y. Peng, J. Zhong, M. Chen, X. Zhao, Z. Deng, *Small* **2021**, *18*, 2106260.
[30] B. Wang, K. Zhao, Z. Yu, C. Sun, Z. Wang, N. Feng, L. Mai, Y. Wang, Y. Xia, *Energy Environ. Sci.* **2020**, *13*, 2200.
[31] K. Sun, X. Wu, Z. Zhuang, L. Liu, J. Fang, L. Zeng, J. Ma, S. Liu, J. Li, R. Dai, X. Tan, K. Yu, D. Liu, W. C. Cheong, A. Huang, Y. Liu, Y. Pan, H. Xiao, C. Chen, *Nat. Commun.* **2022**, *13*, 6260.
[32] Y. Tian, J. Hong, D. Cao, S. You, Y. Song, B. Cheng, Z. Wang, D. Guan, X. Liu, Z. Zhao, X. Z. Li, L. M. Xu, J. Guo, J. Chen, E. G. Wang, Y. Jiang, *Science* **2022**, *377*, 315.
[33] X. Wei, S. Song, W. Cai, X. Luo, L. Jiao, Q. Fang, X. Wang, N. Wu, Z. Luo, H. Wang, Z. Zhu, J. Li, L. Zheng, W. Gu, W. Song, S. Guo, C. Zhu, *Chem* **2023**, *9*, 181.
[34] X. Liu, Y. Wang, J. Liang, S. Li, S. Zhang, D. Su, Z. Cai, Y. Huang, L. Elbaz, Q. Li, *J. Am. Chem. Soc.* **2024**, *146*, 2033.
[35] A. L. Maulana, P. C. Chen, Z. Shi, Y. Yang, C. Lizandara-Pueyo, F. Seeler, H. D. Abruña, D. Muller, K. Schierle-Arndt, P. Yang, *Nano Lett.* **2023**, *23*, 6637.
[36] G. Kresse, J. Furthmüller, *Comput. Mater. Sci.* **1996**, *6*, 15.
[37] J. P. Perdew, K. Burke, M. Ernzerhof, *Phys. Rev. Lett.* **1996**, *77*, 3865.
[38] S. Grimme, *J. Comput. Chem.* **2006**, *27*, 1787.
[39] S. Maintz, V. L. Deringer, A. L. Tchougréeff, R. Dronskowski, *J. Comput. Chem.* **2016**, *37*, 1030.
[40] K. Momma, F. Izumi, *J. Appl. Crystallogr.* **2011**, *44*, 1272.
[41] V. Wang, N. Xu, J. C. Liu, G. Tang, W. T. Geng, *Comput. Phys. Commun.* **2021**, *267*, 108033.